# Vector Vortex Beam Emitter Embedded in a Photonic Chip

Yuan Chen,[1,2] Ke-Yu Xia,[3,4,5,6,*] Wei-Guan Shen,[1,7] Jun Gao,[1,7] Zeng-Quan Yan,[1,7] Zhi-Qiang Jiao,[1,7] Jian-Peng Dou,[1,7] Hao Tang,[1,7] Yan-Qing Lu,[3,4,5,6,†] and Xian-Min Jin[1,7,‡]

[1]*Center for Integrated Quantum Information Technologies (IQIT), School of Physics and Astronomy and State Key Laboratory of Advanced Optical Communication Systems and Networks, Shanghai Jiao Tong University, Shanghai 200240, China*

[2]*Institute for Quantum Science and Engineering and Department of Physics, Southern University of Science and Technology, Shenzhen 518055, China*

[3]*College of Engineering and Applied Sciences, Nanjing University, Nanjing 210093, China*

[4]*National Laboratory of Solid State Microstructures, Collaborative Innovation Center of Advanced Microstructures, Nanjing University, Nanjing 210093, China*

[5]*Jiangsu Key Laboratory of Artificial Functional Materials, Nanjing University, Nanjing 210093, China*

[6]*Key Laboratory of Intelligent Optical Sensing and Manipulation (Nanjing University), Ministry of Education, Nanjing 210093, China*

[7]*CAS Center for Excellence and Synergetic Innovation Center in Quantum Information and Quantum Physics, University of Science and Technology of China, Hefei, Anhui 230026, China*

(Received 26 February 2019; accepted 23 March 2020; published 16 April 2020)

Vector vortex beams simultaneously carrying spin and orbital angular momentum of light promise additional degrees of freedom for modern optics and emerging resources for both classical and quantum information technologies. The inherently infinite dimensions can be exploited to enhance data capacity for sustaining the unprecedented growth in big data and internet traffic and can be encoded to build quantum computing machines in high-dimensional Hilbert space. So far, much progress has been made in the emission of vector vortex beams from a chip surface into free space; however, the generation of vector vortex beams inside a photonic chip has not been realized yet. Here, we demonstrate the first vector vortex beam emitter embedded in a photonic chip by using femtosecond laser direct writing. We achieve a conversion of vector vortex beams with an efficiency up to 30% and scalar vortex beams with an efficiency up to 74% from Gaussian beams. We also present an expanded coupled-mode model for understanding the mode conversion and the influence of the imperfection in fabrication. The fashion of embedded generation makes vector vortex beams directly ready for further transmission, manipulation, and emission without any additional interconnection. Together with the ability to be integrated as an array, our results may enable vector vortex beams to become accessible inside a photonic chip for high-capacity communication and high-dimensional quantum information processing.

DOI: 10.1103/PhysRevLett.124.153601

Light can carry both spin and orbital angular momentum (OAM). Spin angular momentum is associated with optical polarization, which is one of the most prominent and well-known properties of light. OAM is an emerging degree of freedom, which has helical wavefronts described by an azimuthal phase term $e^{i\ell\varphi}$ [1] ($\varphi$ is the azimuthal angle in a cylindrical coordinate system). The topological charge $\ell$ can take any integer value represented by the number of crossed spiral wavefronts when rotating around the axis once. Because of the unlimited topological charges and the inherent orthogonality, OAM can provide larger alphabets for classical information [2–4] and quantum information processing (QIP) [5–11].

Recently, there has been an increasing interest in vector vortex light beams, with a polarization varying along the azimuthal coordinate and a central optical singularity. Such beams exhibit some unique characteristics such as field structure, phase singularity, and rotation invariance [12]. Vector vortex beams have been applied to wide areas including microscopy [13], optical trapping [14], precision measurement [15], quantum communication [12,16], and QIP [17–21].

Large-scale applications beyond proof-of-principle demonstrations require developing integrated techniques to enable the generation [22–26], transmission [27], and even processing of vector vortex beams on a photonic chip. Several pioneering works have demonstrated on-chip generation vector vortex beams with integrated microring resonators [22,23,25,26]. While the emission of vector vortex beams from the surface of integrated devices to free space has been widely investigated, generation and transmission inside a photonic chip remain to be realized and very challenging.

In this Letter, we demonstrate a direct generation of vector vortex beams inside a photonic chip based on mode

 

coupling. By using a femtosecond laser direct writing technique [28–30], we construct a coupled structure consisting of a single-mode waveguide and a doughnut-shaped waveguide. Gaussian beams in the single-mode waveguide evanescently couple to the adjacent OAM waveguide and convert into vector vortex beams according to our coupled-mode model. In addition, we present an integrated array of such emitters and a robust generation of multiple vector vortex beams in the presence of a fluctuation of the writing laser energy.

The prerequisite of generating vector vortex beams inside a photonic chip is that there exists a waveguide supporting OAM modes. The required doughnut-shaped waveguide faithfully mapping twisted light into and out of a photonic chip has been recently achieved [27]. Going beyond a straight doughnut-shaped waveguide and preservation of OAM modes, here we aim to design and construct an asymmetric direction coupler consisting of a standard single-mode waveguide and an OAM waveguide in a photonic chip.

The generation of vector vortex fields in our experiment can be understood by expanding the standard coupled-mode theory [31,32] into the vortex-mode case (see Supplemental Material, Sec. III [33–36]). This model is equivalent to that in Refs. [37,38] but is more transparent in physics. It has been widely used to study the mode coupling between optical resonators [39,40] and waveguides [41].

In an ideally made direction coupler, the single-mode (OAM) waveguide can be defined with its dielectric constant distribution $\varepsilon_s + \varepsilon_a$ ($\varepsilon_s + \varepsilon_b$), where $\varepsilon_s$ is the dielectric constant of the substrate and $\varepsilon_a$ ($\varepsilon_b$) the wanted change, symmetric around the $z$ axis, induced by the writing laser beam. Ideally, the modes in these two waveguides have the same propagation constant $\bar{\beta}$. Because of the deviation of the laser energy from an axial symmetrical profile, the single-mode (OAM) waveguide has birefringence due to perturbation $\Delta\varepsilon_a$ ($\Delta\varepsilon_b$), which are tensors (see Supplemental Material, Sec. III [33–36]). The envelope of field in the chip can be expanded to the superposition of eigenmodes as $\tilde{\mathbf{E}} = \sum_m \tilde{A}_m \tilde{\mathbf{E}}_m^G + \sum_n \tilde{B}_n \tilde{\mathbf{E}}_n^{\mathrm{OAM}}$, where $\tilde{A}_m$ ($\tilde{B}_n$) is the amplitude of the $m$th ($n$th) eigenmode $\tilde{\mathbf{E}}_m^G$ ($\tilde{\mathbf{E}}_n^{\mathrm{OAM}}$) with propagation constant $\beta_m^G$ ($\beta_n^{\mathrm{OAM}}$) in the single-mode (OAM) waveguide. $\tilde{\mathbf{E}}_m^G$ can be $\tilde{\mathbf{E}}_{G_{x'}}^G$ or $\tilde{\mathbf{E}}_{G_{y'}}^G$. $\tilde{\mathbf{E}}_n^{\mathrm{OAM}}$ can be $\tilde{\mathbf{E}}_{x_\ell}^{\mathrm{OAM}}$, $\tilde{\mathbf{E}}_{x_{-\ell}}^{\mathrm{OAM}}$, $\tilde{\mathbf{E}}_{y_\ell}^{\mathrm{OAM}}$, or $\tilde{\mathbf{E}}_{y_{-\ell}}^{\mathrm{OAM}}$ with $\pm\ell\hbar$ OAM. For convenience, we have omitted the superscript $G$ (OAM) representing Gaussian (OAM) modes in the single-mode (OAM) waveguide associated with subscript $m$ ($n$) in the following expressions.

Starting from Maxwell's equations, we derive the general coupled-mode equations (see Supplemental Material, Sec. III [33–36])

$$j\frac{\partial \tilde{A}_{m'}}{\partial z} = \Delta\beta_{m'}\tilde{A}_{m'} + \sum_{m\neq m'} h_{m,m'}\tilde{A}_m + \sum_n \kappa_{n,m'}\tilde{B}_n, \quad (1a)$$

$$j\frac{\partial \tilde{B}_{n'}}{\partial z} = \Delta\beta_{n'}\tilde{B}_{n'} + \sum_{n\neq n'} h_{n,n'}\tilde{B}_n + \sum_m \kappa_{m,n'}\tilde{A}_m, \quad (1b)$$

where $\Delta\beta_{m'} = \beta_{m'} - \bar{\beta} + \delta_{m'}$ and $\Delta\beta_{n'} = \beta_{n'} - \bar{\beta} + \delta_{n'}$. Ideally, $\beta_{m'} = \bar{\beta}$ and $\beta_{n'} = \bar{\beta}$. Here, we neglect the Butt couplings, because they are orders smaller than the shifts and other couplings. The propagation constant shifts $\delta_{m'}$ ($\delta_{n'}$), the couplings $h_{m,m'}$ ($h_{n,n'}$) between the eigenmodes in the single-mode (OAM) waveguide, and the couplings $\kappa_{n,m'}$ ($\kappa_{m,n'}$) between the waveguides are given by

$$\delta_X = \frac{k_0^2}{2\beta_X N_X}\int \tilde{\mathbf{E}}_X^* \cdot (\varepsilon_p + \Delta\varepsilon_b + \Delta\varepsilon_a)\cdot \tilde{\mathbf{E}}_X dxdy, \quad (2a)$$

$$h_{Y,X} = \frac{k_0^2}{2\beta_X N_X}\int \tilde{\mathbf{E}}_X^* \cdot (\varepsilon_p + \Delta\varepsilon_b + \Delta\varepsilon_a)\cdot \tilde{\mathbf{E}}_Y dxdy, \quad (2b)$$

where $\int \tilde{\mathbf{E}}_X \cdot \tilde{\mathbf{E}}_X^* dxdy = N_X$ and $\{X, Y, p\} = \{m', m, b\}$ ($\{X, Y, p\} = \{n', n, a\}$) for the single-mode (OAM) waveguide, and

$$\kappa_{Y,X} = \frac{k_0^2}{2\beta_X N_X}\int \tilde{\mathbf{E}}_X^* \cdot (\varepsilon_p + \Delta\varepsilon_a + \Delta\varepsilon_b)\cdot \tilde{\mathbf{E}}_Y dxdy, \quad (3)$$

where $\{X, Y, p\} = \{m', n, a\}$ ($\{X, Y, p\} = \{n', m, b\}$) and $k_0$ is the propagation constant of light in free space. Obviously, the birefringence resulting from $\Delta\varepsilon_a$ and $\Delta\varepsilon_b$ changes the propagation constant shifts and all coupling coefficients.

Gaussian beams in the single-mode waveguide can be evanescently coupled to the adjacent doughnut-shaped waveguide and converted into vector vortex beams according to our coupled-mode theory [see Fig. 1(a)]. However, the complete modal conversion can happen only under $\Delta\beta_{m',n'} = \beta_{m'} - \beta_{n'} = 0$ [42]. Note that $\beta_{m'}$ ($\beta_{n'}$) is mode dependent. Therefore, the phase matching condition should be subject to exciting the specific order of vector vortex beams. Instead of propagation constants $\beta_{m'}$ and $\beta_{n'}$, we choose more convenient effective refractive index $n_{\mathrm{eff}} = \beta/k$. In our experiment, we fix the size of the single-mode waveguide and tune the effective refractive index via changing the size of the OAM waveguide [42–46]. The OAM waveguide structure with radius $R$ is shown in Fig. 1(b).

To find the optimal radius at which Gaussian modes are phase matched with vortex modes, we calculate the effective refractive indices for different orders of vortex modes [42,46] [see Fig. 1(c)]. The phase matching graph indicates that the OAM waveguide should be written with a radius of around 3.5 $\mu$m (4.9 $\mu$m), which can match Gaussian modes to generate first-order (second-order) vortex modes. The calculated results are instructive; however, since the fabrication and coupling of two different types of waveguides are involved and laser-matter interaction is quite complicated with many involved physical

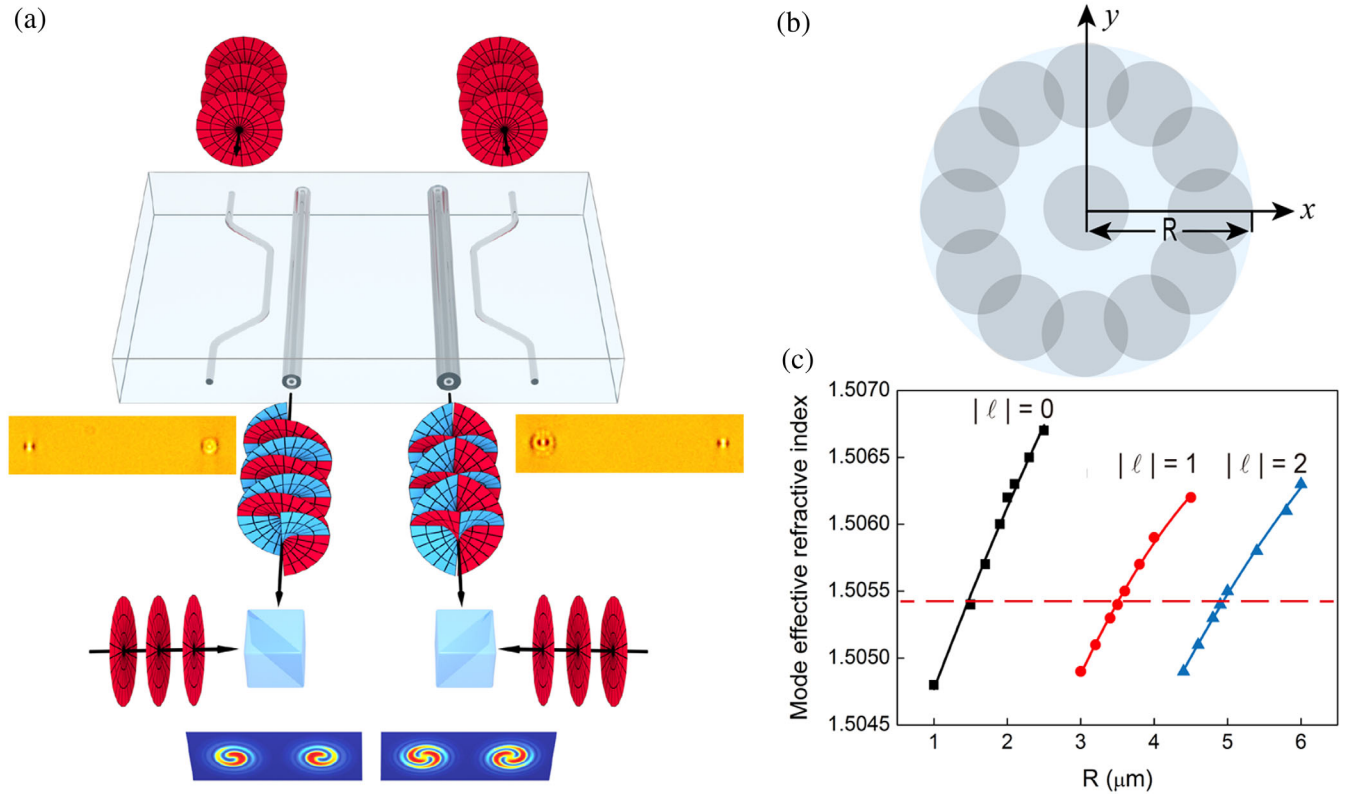


FIG. 1. Experimental principle of generating vortex modes in a photonic chip. (a) An asymmetric direction coupler consisting of a standard single-mode waveguide and an OAM waveguide is employed to generate different order vortex beams based on phase matching. The coupling spacing and coupling length are 15 $\mu$m and 4 mm, respectively. A Ti:sapphire oscillator centered at 780 nm is divided into two beams by inserting a beam splitter. One of the Gaussian beams is utilized as the incident light to generate vector vortex beams. The second one serves as the reference beam to measure the interference patterns with the generated vector vortex beam. A translation stage is added to tune the phase for high-contrast interference fringes, and a CCD is used to record the patterns. The insets show the cross-section images of a femtosecond laser-written asymmetric direction coupler. (b) Illustration of the OAM waveguide structure. Twelve tracks constitute the annular structure with a radius $R$, and they are overlapped to form a continuous refractive index distribution. The doughnut-shaped structure will consist of 13 waveguides when we apply an additional scan through the middle. (c) The phase matching graph for the Gaussian modes and different order vortex modes. The black, red, and blue dotted lines correspond to Gaussian modes and first-order and second-order vortex modes, respectively. The horizontal red dashed line shows the phase matching for waveguides with different sizes to generate different order vortex beams.

processes [29,30], a detailed scan of the size of the OAM waveguide near the estimated value is essential to achieve an efficient mode conversion. Finally, we obtained high-quality first-order and second-order vortex modes at $R \simeq 3.7$ $\mu$m and $R \simeq 5.0$ $\mu$m, respectively.

To analyze the evolution of field in the OAM waveguide, we divide the asymmetric direction coupler into three segments: the input ($0 \le z \le L_1$), coupling ($L_1 \le z \le L_1 + L_{cp}$), and output ($L_1 + L_{cp} \le z \le L$) regions, where $L$ is the length of chip. In the input and output regions, the two waveguides are uncoupled. However, due to the nonzero $\Delta\varepsilon_a$ and $\Delta\varepsilon_b$, the field changes during propagating in these regions. The modes in two waveguides interact with each other in the coupling region. The evolution of field can be described by Eq. (1).

The incident Gaussian field can be written as $\mathbf{E}_{\text{in}}(0) = \tilde{A}_{G_{x'}}(0)\tilde{\mathbf{E}}_{G_{x'}} + \tilde{A}_{G_{y'}}(0)\tilde{\mathbf{E}}_{G_{y'}}$. The field can be determined by the input and the evolution matrix $M$ (see Supplemental Material, Sec. IV [33]), which is dependent on the structure of the waveguides and is a function of $\Delta\beta_{m'}$, $\Delta\beta_{n'}$, $h_{m,m'}$, $h_{n,n'}$, $\kappa_{n,m'}$, and $\kappa_{m,n'}$ (see Supplemental Material, Sec. III [33–36]). The output field can also be expanded as the superposition of eigenmodes in the OAM waveguide as $\tilde{\mathbf{E}}(L) = \gamma_{x_\ell}\tilde{\mathbf{E}}_{x_\ell} + \gamma_{x_{-\ell}}\tilde{\mathbf{E}}_{x_{-\ell}} + \gamma_{y_\ell}\tilde{\mathbf{E}}_{y_\ell} + \gamma_{y_{-\ell}}\tilde{\mathbf{E}}_{y_{-\ell}}$, with

$$\begin{bmatrix} \gamma_{x_\ell} \\ \gamma_{x_{-\ell}} \\ \gamma_{y_\ell} \\ \gamma_{y_{-\ell}} \end{bmatrix}^T = \begin{bmatrix} \tilde{A}_{G_{x'}}(0) \\ \tilde{A}_{G_{y'}}(0) \\ 0 \\ 0 \end{bmatrix}^T M_1^T(L_1) M_{cp}^T(L_{cp}) M_2^T(L_2), \quad (4)$$

where $\tilde{\mathbf{E}}_{x_{\pm\ell}} = E_{x_{\pm\ell}} e^{\pm j\ell\phi}\mathbf{e}_x$, $\tilde{\mathbf{E}}_{y_{\pm\ell}} = E_{y_{\pm\ell}} e^{\pm j\ell\phi}\mathbf{e}_y$, $M_1$ ($M_2$, $M_{cp}$) describes the evolution of field in the input (output,

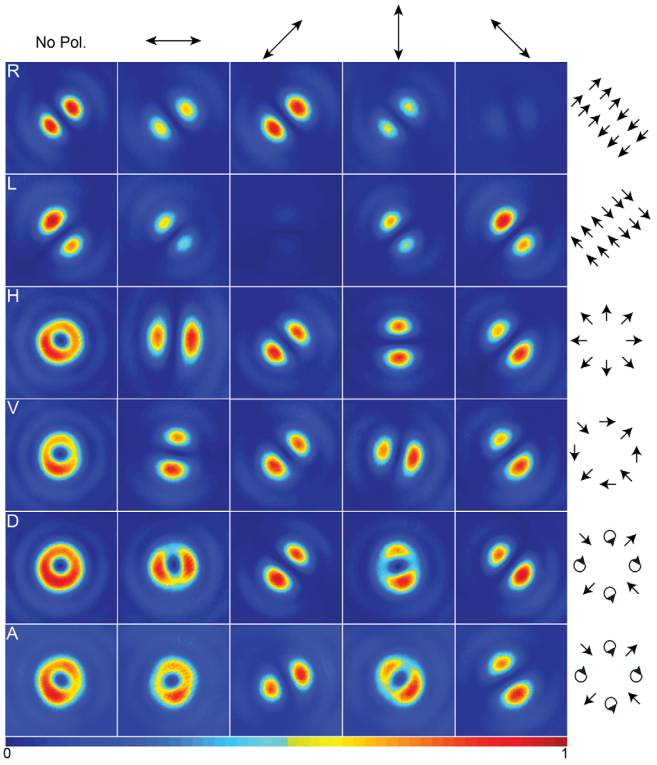


FIG. 2. Experimental results of generating first-order vortex beams. Measured intensity distribution for right-circularly (left-circularly, horizontally, vertically, diagonally, and antidiagonally) polarized Gaussian beams and the corresponding intensity distributions after polarization analysis are shown in the first (second, third, fourth, fifth, and sixth, respectively) row. The direction of polarization projection is indicated by the arrows, and the spatial polarization distribution is shown at the end of each row. The resulting modes have different spatial polarization distributions for different input polarized Gaussian beams, which suggests there exists birefringence in the doughnut-shaped waveguide.

coupling, respectively) region, and $T$ means the transpose of a matrix.

When right-circularly polarized Gaussian beams incident and evanescently couple into the OAM waveguide, a two-lobe intensity distribution is obtained (see Fig. 2). After projecting to horizontal and vertical polarization, the two-lobe intensity distribution in the near-diagonal direction suggests that $\gamma_{x_{-\ell}}E_{x_{-\ell}} \simeq j\gamma_{x_\ell}E_{x_\ell}$ and $\gamma_{y_{-\ell}}E_{y_{-\ell}} \simeq j\gamma_{y_\ell}E_{y_\ell}$. Note that the intensity after antidiagonal polarization projection is relatively small comparing with diagonal polarization with an extinction ratio up to 10.2 dB observed in the experiment. Obviously, this is a scalar light field with diagonal polarization. The small component on the antidiagonal polarization means $\tilde{\mathbf{E}}(L)\cdot\mathbf{e}_a \simeq 0$, so that $\gamma_{y_\ell}E_{y_\ell} \simeq \gamma_{x_\ell}E_{x_\ell}$ (see Supplemental Material, Sec. IV [33]).

With an input of a left-circularly polarized Gaussian beam, the generated vortex beam also exhibits a scalar light field with antidiagonal polarization. Although the intensity distribution is uneven, the two lobes near the antidiagonal direction after respectively projecting to horizontal and vertical polarization indicate that $\gamma_{x_{-\ell}}E_{x_{-\ell}} \simeq -j\gamma_{x_\ell}E_{x_\ell}$ and $\gamma_{y_{-\ell}}E_{y_{-\ell}} \simeq -j\gamma_{y_\ell}E_{y_\ell}$. The intensity after diagonal polarization projection is relatively small comparing with antidiagonal polarization with an extinction ratio up to 9.6 dB. The component with diagonal polarization is $\tilde{\mathbf{E}}(L)\cdot\mathbf{e}_d \simeq 0$, meaning $\gamma_{y_\ell}E_{y_\ell} \simeq -\gamma_{x_\ell}E_{x_\ell}$ (see Supplemental Material, Sec. IV [33]).

When the asymmetric direction coupler is excited by horizontally polarized Gaussian beams, we obtain good circularly symmetric first-order vector vortex modes, whose intensity distributions are annular with a dark core in the center. Projecting the generated beam to different polarizations with a polarizer, the two-lobe pattern is formed and rotates with the polarizer, which implies that it is a cylindrical vector vortex beam with radial polarization [24,47,48]. This experimental result manifests that $\gamma_{x_{-\ell}}E_{x_{-\ell}} \simeq \gamma_{x_\ell}E_{x_\ell}$, $\gamma_{y_{-\ell}}E_{y_{-\ell}} \simeq -\gamma_{y_\ell}E_{y_\ell}$, and $\gamma_{y_\ell}E_{y_\ell} \simeq -j\gamma_{x_\ell}E_{x_\ell}$ (see Supplemental Material, Sec. IV [33]).

Similarly, we generate a $\pi$-vector vortex beam [14,20] by coupling a vertically polarized Gaussian beam into the doughnut-shaped waveguide. Our polarization analysis [48,49] indicates that the vector vortex mode is linearly polarized at each local position but with a local polarization direction changing between radial and azimuthal direction (see Fig. 2). We also find that when injecting a diagonally (antidiagonally) polarized Gaussian beam, the generated mode shows an annular intensity distribution when projected to horizontal and vertical polarization, while it shows a two-lobe intensity distribution when projected to a diagonal and antidiagonal polarization. The resulting modes have different spatial polarization distributions for Gaussian beams with different input polarizations, which suggests there exists birefringence in the doughnut-shaped waveguide.

A variation of the coupling between the waveguides by changing the energy of the writing laser have been observed in Fig. 3, which can be reflected into a change in the propagation constant. Our theory, in good agreement with previous experiments [50,51], shows that this change is linearly dependent on the energy variation of the writing laser (see Supplemental Material, Sec. I [33,52,53]).

When we increase the pulse energy, the distribution of optical axis has no substantial change (see Supplemental Material, Sec. II [33]), and the conversion efficiency of first-order vortex modes increases from 42.2% to 74.2% [see Fig. 3(a)]. Meanwhile, the resulting modes become pure scalar vortex modes. We can see that the generated modes are all good vector vortex modes in a range of writing pulse energy. We further perform a comprehensive polarization analysis on the typical states ($B$, $D$, and $F$) generated with different pulse energies [see Fig. 3(b)]. We can observe a clear trend to single-polarization vortex beams and a high extinction ratio at a high writing pulse energy ($F$).

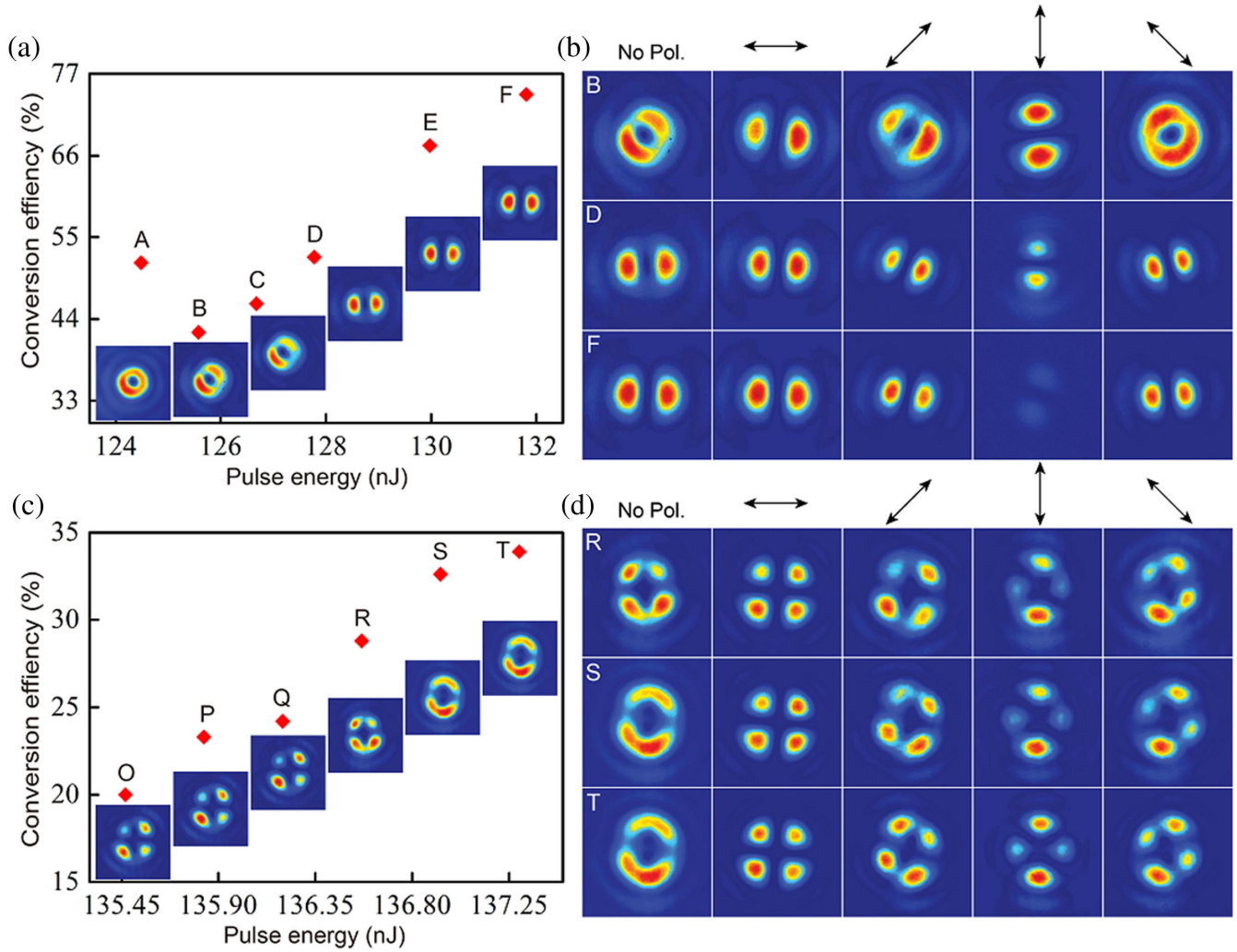


FIG. 3. The evolution of resulting vortex modes when increasing the writing pulse energy. (a) Conversion efficiency and first-order vortex modes versus the writing pulse energy. (b) The polarization analysis on the typical states $B$, $D$, and $F$. It is obvious that, when we increase the pulse energy, the resulting beam changes from vector vortex to scalar vortex. (c) Conversion efficiency and second-order vortex modes versus the writing pulse energy. (d) The polarization analysis on the typical states $R$, $S$, and $T$. The direction of polarization projection is indicated by the arrows.

By increasing the radius of the doughnut-shaped waveguide, we can tune the phase matching condition for second-order vortex modes [see Fig. 3(c)]. We find that there also exists a sweet spot of the writing pulse energy, where second-order vector vortex beams can be well observed and the conversion efficiency can be optimized before apparently becoming a scalar vortex beam. Before the efficiency reaches 33.9%, the polarization analysis on $R$, $S$, and $T$ reveals no distinct changes of polarization distribution [see Fig. 3(d)].

To demonstrate the potential toward large-scale integration, we construct an array consisting of three such asymmetric directional couplers as first-order and second-order vector vortex beam emitters, respectively [see Fig. 4(a)]. Owing to the complex physical process of femtosecond laser micromachining, many parameters have been found strongly affecting the resulting morphology and, therefore, the characteristics of waveguides [30]. To keep all the waveguides identical, we lock all the parameters of the laser, the translation stages, and the environment. We show that, even with an artificially introduced fluctuation, about 1.465 nJ (0.4 nJ) in generating first-order (second-order) vector vortex beams, we still can obtain almost identical emission [see Figs. 4(b) and 4(c)]. The expected clockwise or counterclockwise spiral interference patterns clearly identify the ingredient of three output states in first- and second-order vector vortex modes. We extract the radial intensity distribution from the first- and second-order modes along the white radial direction [see Figs. 4(d) and 4(e)]. The relatively balanced intensity distribution once again implies a robust generation of vortex beams against the fluctuation of the writing laser energy.

In summary, we demonstrated the first vector vortex beam emitter embedded in a photonic chip by using femtosecond

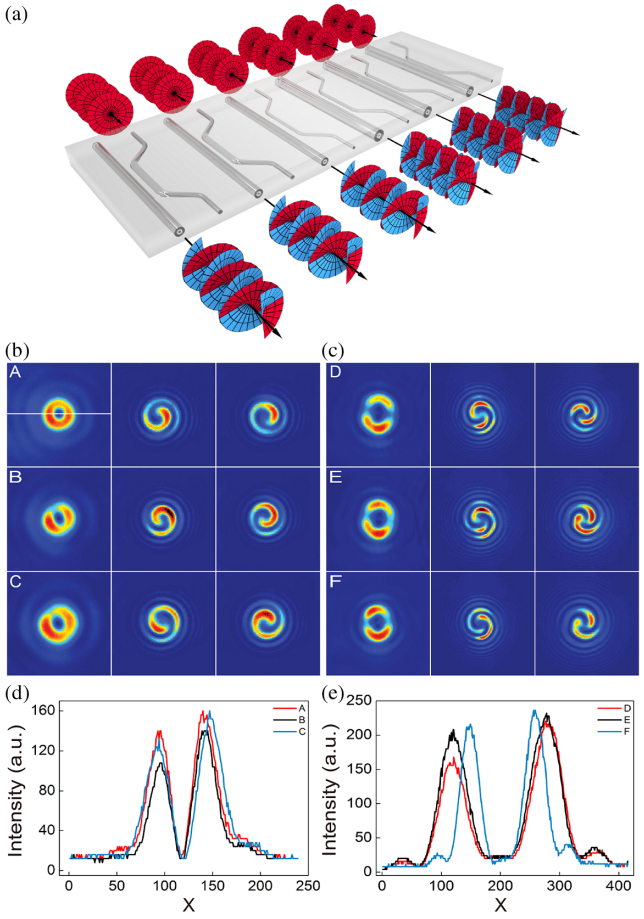


FIG. 4. Experimental results of vortex beam emitter array. (a) Illustration of an array consisting of three asymmetric directional couplers for first- and second-order vector vortex beam emitters, respectively. (b) The first column: intensity patterns generated from the first-order vortex beam array. The difference in their shape can be attributed to slight differences in the writing pulse energy and fabrication variations. The clockwise (counterclockwise) spiral interference patterns with one arm are shown in the second (third) column for first-order vector vortex beams. (c) The first column: intensity patterns generated from the second-order vortex beam array. The clockwise (counterclockwise) spiral interference patterns with two arms are shown in the second (third) column. Even with an artificially introduced energy fluctuation of the write beam, about 1.465 nJ (0.4 nJ) in generating first-order (second-order) vector vortex beams, we still can obtain almost identical emission and a robust generation of multiple vector vortex beams against the fluctuation of the writing laser energy. (d) Radial intensity distribution extracted from the first-order vortex beam along the white radial direction corresponds to *A*, *B*, and *C*. (e) Radial intensity distribution extracted from the second-order vortex beam *D*, *E*, and *F*.

laser direct writing. By engineering the phase matching condition, we generated the first- and second-order vector vortex beams with optical chirality and achieved very high conversion efficiency by tuning the writing pulse energy. The fashion of embedded generation makes vector vortex beams directly ready for further transmission, manipulation, and emission without any additional interconnection. We also demonstrated an integrated array of such emitters and a robust generation of multiple vector vortex beams, which is crucial toward high-capacity communication and high-dimensional [54,55] QIP.

This emerging field of integrated photonics of vector vortex beams has many open problems to be addressed. The evanescent light coupling or splitting between two vector vortex waveguides is a primary goal, which may facilitate the design and fabrication of many novel integrated devices of vector vortex beams, and especially may enable on-chip quantum interference of vector vortex beams. Quantum inference between the transverse spatial modes has been observed in multimode waveguides [46], opening the possibility to realize on-chip Hong-Ou-Mandel interference for vector vortex modes [56]. The efficient generation of pure scalar vortex modes in our experiment promises the potential for preparing indistinguishable vortex photonic states and observing the interference with high visibility. In addition, introducing chiral structure to the OAM waveguide may allow controllably generate certain chiral vortex states.

The authors thank Miles Padgett, Nathan Langford, Si-Yuan Yu, and Jian-Wei Pan for helpful discussions. This work was supported by National Key R&D Program of China (2019YFA0308700 and 2017YFA0303700); National Natural Science Foundation of China (NSFC) (61734005, 11761141014, 11690033, 11890704, and 11874212); Science and Technology Commission of Shanghai Municipality (STCSM) (17JC1400403); Shanghai Municipal Education Commission (SMEC) (2017-01-07-00-02-E00049); X.-M. J. acknowledges additional support from a Shanghai talent program.

*keyu.xia@nju.edu.cn
†yqlu@nju.edu.cn
‡xianmin.jin@sjtu.edu.cn

[1] L. Allen, M. W. Beijersbergen, R. J. C. Spreeuw, and J. P. Woerdman, Orbital angular momentum of light and the transformation of Laguerre-Gaussian laser modes, Phys. Rev. A **45**, 8185 (1992).
[2] J. Wang *et al.*, Terabit free-space data transmission employing orbital angular momentum multiplexing, Nat. Photonics **6**, 488 (2012).
[3] N. Bozinovic, Y. Yue, Y. Ren, M. Tur, P. Kristensen, H. Huang, A. E. Willner, and S. Ramachandran, Terabit-scale orbital angular momentum mode division multiplexing in fibers, Science **340**, 1545 (2013).
[4] A. E. Willner *et al.*, Optical communications using orbital angular momentum beams, Adv. Opt. Photonics **7**, 66 (2015).
[5] J. T. Barreiro, T.-C. Wei, and P. G. Kwiat, Beating the channel capacity limit for linear photonic superdense coding, Nat. Phys. **4**, 282 (2008).

[6] A. C. Dada, J. Leach, G. S. Buller, M. J. Padgett, and E. Andersson, Experimental high dimensional two-photon entanglement and violations of generalized Bell inequalities, Nat. Phys. **7**, 677 (2011).
[7] R. Fickler, R. Lapkiewicz, W. N. Plick, M. Krenn, C. Schaeff, S. Ramelow, and A. Zeilinger, Quantum entanglement of high angular momenta, Science **338**, 640 (2012).
[8] M. Krenn, M. Huber, R. Fickler, R. Lapkiewicz, S. Ramelow, and A. Zeilinger, Generation and confirmation of a $(100 \times 100)$-dimensional entangled quantum system, Proc. Natl. Acad. Sci. U.S.A. **111**, 6243 (2014).
[9] M. Mirhosseini, O. S Magaña-Loaiza, M. N. O'Sullivan, B. Rodenburg, M. Malik, M. P. J. Lavery, M. J. Padgett, D. J. Gauthier, and R. W. Boyd, High-dimensional quantum cryptography with twisted light, New J. Phys. **17**, 033033 (2015).
[10] F. Bouchard, R. Fickler, R. W. Boyd, and E. Karimi, High-dimensional quantum cloning and applications to quantum hacking, Sci. Adv. **3**, e1601915 (2017).
[11] D. Cozzolino *et al.*, Orbital Angular Momentum States Enabling Fiber-Based High-Dimensional Quantum Communication, Phys. Rev. Applied **11**, 064058 (2019).
[12] V. D'Ambrosio, E. Nagali, S. P. Walborn, L. Aolita, S. Slussarenko, L. Marrucci, and F. Sciarrino, Complete experimental toolbox for alignment-free quantum communication, Nat. Commun. **3**, 961 (2012).
[13] A. F. Abouraddy and K. C. Toussaint, Jr., Three-Dimensional Polarization Control in Microscopy, Phys. Rev. Lett. **96**, 153901 (2006).
[14] B. J. Roxworthy and K. C. Toussaint, Jr., Optical trapping with $\pi$-phase cylindrical vector beams, New J. Phys. **12**, 073012 (2010).
[15] V. D'Ambrosio, N. Spagnolo, L. Del Re, S. Slussarenko, Y. Li, L. Chuan Kwek, L. Marrucci, S. P. Walborn, L. Aolita, and F. Sciarrino, Photonic polarization gears for ultrasensitive angular measurements, Nat. Commun. **4**, 2432 (2013).
[16] G. Vallone, V. D'Ambrosio, A. Sponselli, S. Slussarenko, L. Marrucci, F. Sciarrino, and P. Villoresi, Free-Space Quantum Key Distribution by Rotation-Invariant Twisted Photons, Phys. Rev. Lett. **113**, 060503 (2014).
[17] J. T. Barreiro, T.-C. Wei, and P. G. Kwiat, Remote Preparation of Single-Photon "Hybrid" Entangled and Vector-Polarization States, Phys. Rev. Lett. **105**, 030407 (2010).
[18] R. Fickler, R. Lapkiewicz, S. Ramelow, and A. Zeilinger, Quantum entanglement of complex photon polarization patterns in vector beams, Phys. Rev. A **89**, 060301(R) (2014).
[19] V. Parigi, V. D'Ambrosio, C. Arnold, L. Marrucci, F. Sciarrino, and J. Laurat, Storage and retrieval of vector beams of light in a multiple-degree-of-freedom quantum memory, Nat. Commun. **6**, 7706 (2015).
[20] V. D'Ambrosio, G. Carvacho, F. Graffitti, C. Vitelli, B. Piccirillo, L. Marrucci, and F. Sciarrino, Entangled vector vortex beams, Phys. Rev. A **94**, 030304(R) (2016).
[21] D. Cozzolino, E. Polino, M. Valeri, G. Carvacho, D. Bacco, N. Spagnolo, L. K. K. Oxenløwe, and F. Sciarrino, Air-core fiber distribution of hybrid vector vortex-polarization entangled states, Adv. Opt. Photonics **1**, 046005 (2019).
[22] X.-L. Cai, J. Wang, M. J. Strain, B. Johnson-Morris, J. Zhu, M. Sorel, J. L. O'Brien, M. G. Thompson, and S. Yu, Integrated compact optical vortex beam emitters, Science **338**, 363 (2012).
[23] S. A. Schulz, T. Machula, E. Karimi, and R. W. Boyd, Integrated multi vector vortex beam generator, Opt. Express **21**, 16130 (2013).
[24] D. Naidoo, F. S. Roux, A. Dudley, I. Litvin, B. Piccirillo, L. Marrucci, and A. Forbes, Controlled generation of higher-order Poincaré sphere beams from a laser, Nat. Photonics **10**, 327 (2016).
[25] Z.-K. Shao, J. Zhu, Y. Zhang, Y. Chen, and S. Yu, On-chip switchable radially and azimuthally polarized vortex beam generation, Opt. Lett. **43**, 1263 (2018).
[26] J. Liu *et al.*, Direct fiber vector eigenmode multiplexing transmission seeded by integrated optical vortex emitters, Light Sci. Appl. **7**, 17148 (2018).
[27] Y. Chen, J. Gao, Z. Q. Jiao, K. Sun, W. G. Shen, L. F. Qiao, H. Tang, X. F. Lin, and X. M. Jin, Mapping Twisted Light Into and Out of a Photonic Chip, Phys. Rev. Lett. **121**, 233602 (2018).
[28] R. R. Gattass, and E. Mazur, Femtosecond laser micromachining in transparent materials, Nat. Photonics **2**, 219 (2008).
[29] A. Szameit, and S. Nolte, Discrete optics in femtosecond-laser-written photonic structures, J. Phys. B **43**, 163001 (2010).
[30] R. Osellame *et al.*, *Femtosecond Laser Micromachining: Photonic and Microfluidic Devices in Transparent Materials* (Springer, New York, 2012).
[31] E. Marcatili, Improved coupled-mode equations for dielectric guides, IEEE J. Quantum Electron. **22**, 988 (1986).
[32] M. Borselli, T. J. Johnson, and O. Painter, Beyond the Rayleigh scattering limit in high-Q silicon microdisks: Theory and experiment, Opt. Express **13**, 1515 (2005).
[33] See Supplemental Material at http://link.aps.org/supplemental/10.1103/PhysRevLett.124.153601 for Sec. I, the relationship between the writing laser energy and the propagation constant, which includes Refs. [52–53], Sec. II, the optical axis distribution of the OAM waveguide, Sec. III, a general coupled-mode equation derivation including six eigenmodes, which includes Refs. [34–36], and Sec. IV, analyzing the evolution of the field in the OAM waveguide.
[34] H. Haus, W. Huang, S. Kawakami, and N. Whitaker, Coupled-mode theory of optical waveguides, J. Lightwave Technol. **5**, 16 (1987).
[35] A. Weierholt, A. Mickelson, and S. Neegard, Eigenmode analysis of symmetric parallel waveguide couplers, IEEE J. Quantum Electron. **23**, 1689 (1987).
[36] G. Corrielli, A. Crespi, R. Geremia, R. Ramponi, L. Sansoni, A. Santinelli, P. Mataloni, F. Sciarrino, and R. Osellame, Rotated waveplates in integrated waveguide optics, Nat. Commun. **5**, 4249 (2014).
[37] W.-P. Huang, Coupled-mode theory for optical waveguides: An overview, J. Opt. Soc. Am. A **11**, 963 (1994).
[38] K. Okamoto, *Fundamentals of Optical Waveguides* (Academic, San Diego, 2006).
[39] K. Srinivasan and O. Painter, Mode coupling and cavity-quantum-dot interactions in a fiber-coupled microdisk cavity, Phys. Rev. A **75**, 023814 (2007).

[40] S. I. Schmid, K. Xia, and J. Evers, Pathway interference in a loop array of three coupled microresonators, Phys. Rev. A **84**, 013808 (2011).

[41] K.-Y. Xia, M. Alamri, and M. Suhail Zubairy, Ultrabroadband nonreciprocal transverse energy flow of light in linear passive photonic circuits, Opt. Express **21**, 25619 (2013).

[42] R. Ismaeel, T. Lee, B. Oduro, Y. Jung, and G. Brambilla, All-fiber fused directional coupler for highly efficient spatial mode conversion, Opt. Express **22**, 11610 (2014).

[43] L.-W. Luo, N. Ophir, C. P. Chen, L. H. Gabrielli, C. B. Poitras, K. Bergmen, and M. Lipson, WDM-compatible mode-division multiplexing on a silicon chip, Nat. Commun. **5**, 3069 (2014).

[44] J. Wang, P. Chen, S. Chen, Y. Shi, and D. Dai, Improved 8-channel silicon mode demultiplexer with grating polarizers, Opt. Express **22**, 12799 (2014).

[45] Y.-D. Yang, Y. Li, Y.-Z. Huang, and A. W. Poon, Silicon nitride three-mode division multiplexing and wavelength-division multiplexing using asymmetrical directional couplers and microring resonators, Opt. Express **22**, 22172 (2014).

[46] A. Mohanty, M. Zhang, A. Dutt, S. Ramelow, P. Nussenzveig, and M. Lipson, Quantum interference between transverse spatial waveguide modes, Nat. Commun. **8**, 14010 (2017).

[47] R. Dorn, S. Quabis, and G. Leuchs, Sharper Focus for a Radially Polarized Light Beam, Phys. Rev. Lett. **91**, 233901 (2003).

[48] C. Maurer, A. Jesacher, S. Fürhapter, S. Bernet, and M. Ritsch-Marte, Tailoring of arbitrary optical vector beams, New J. Phys. **9**, 78 (2007).

[49] F. Cardano, E. Karimi, S. Slussarenko, L. Marrucci, C. de Lisio, and E. Santamato, Polarization pattern of vector vortex beams generated by q-plates with different topological charges, Appl. Opt. **51**, C1 (2012).

[50] R. Diener, S. Nolte, T. Pertsch, and S. Minardi, Effects of stress on neighboring laser written waveguides in gallium lanthanum sulfide, Appl. Phys. Lett. **112**, 111908 (2018).

[51] H. Tang *et al.*, Experimental Quantum Stochastic Walks Simulating Associative Memory of Hopfield Neural Networks, Phys. Rev. Applied **11**, 024020 (2019).

[52] S. Rajesh and Y. Bellouard, Towards fast femtosecond laser micromachining of fused silica: The effect of deposited energy, Opt. Express **18**, 21490 (2010).

[53] M. Lebugle, M. Gräfe, R. Heilmann, A. Perez-Leija, S. Nolte, and A. Szameit, Experimental observation of NooN state Bloch oscillations, Nat. Commun. **6**, 8273 (2015).

[54] M. Malik, M. Erhard, M. Huber, M. Krenn, R. Fickler, and A. Zeilinger, Multi-photon entanglement in high dimensions, Nat. Photonics **10**, 248 (2016).

[55] M. Erhard, R. Fickler, M. Krenn, and A. Zeilinger, Twisted photons: New quantum perspectives in high dimensions, Light Sci. Appl. **7**, 17146 (2018).

[56] V. D'Ambrosio, G. Carvacho, I. Agresti, L. Marrucci, and F. Sciarrino, Tunable Two-Photon Quantum Interference of Structured Light, Phys. Rev. Lett. **122**, 013601 (2019).